



ELSEVIER

Available online at [www.sciencedirect.com](http://www.sciencedirect.com)

SciVerse ScienceDirect

Scripta Materialia 68 (2013) 805–808

[www.elsevier.com/locate/scriptamat](http://www.elsevier.com/locate/scriptamat)

## On dislocation involvement in Ti–Nb gum metal plasticity

E. Plancher, C.C. Tasan,\* S. Sandloebes and D. Raabe

*Max-Planck-Institut für Eisenforschung, Max-Planck-Straße 1, 40237 Düsseldorf, Germany*

Received 17 December 2012; revised 29 January 2013; accepted 29 January 2013

Available online 5 February 2013

The excellent mechanical properties of the Ti–Nb-based gum metal were originally proposed to arise from a “dislocation-free” giant fault mechanism; however, the involvement of lattice dislocations in the process is still under debate. To address this issue, gum metal deformation mechanisms are investigated systematically on cast specimens, employing postmortem and in situ analysis techniques. The results demonstrate that a giant fault mechanism (which appears to be a phase-transformation-assisted nanotwinning mechanism) governs gum metal plasticity without direct assistance from dislocations during the process.  
© 2013 Acta Materialia Inc. Published by Elsevier Ltd. All rights reserved.

**Keywords:** Gum metal; Dislocation; Giant fault; Beta titanium; In situ

“Gum metal” is a recently developed class of beta (i.e. body-centered cubic) titanium-based alloys [1–3], which possesses an excellent yet unusual mechanical behavior: at room temperature, when deformed in tension, gum metal exhibits high yield stress (up to 1 GPa [3,4]) and outstanding elongation to failure (up to 35% [this work]). Despite the rapidly growing interest in this alloy class, the physical mechanisms governing its plastic behavior are still unclear. Specifically, the contribution of lattice dislocation activity in relation to the proposed “giant fault” mechanism is not yet established.

The concept of a giant fault was introduced by the research group that invented and studied the alloy in 2003. Their observations [1–3], and those of others [4,5], revealed the existence of micrometer-sized two-dimensional band-like features carrying local shear. These faults were suggested to correlate with certain crystallographic directions ( $\langle 111 \rangle$ ) that were elastically softened by a careful choice of chemical stoichiometry: Ti–23Nb–0.7Ta–2Zr–1.2O (at.%) [6,7]. Based on reports observing no significant dislocation activity in the alloy [1–3,5,8], some theories have been proposed which support the dislocation-free nature of the giant fault mechanism [9,10].

In contrast to these observations, an increasing number of studies underline the presence and activity of dislocations in gum metal [11–16]. Some studies even claim a fully  $\frac{1}{2}\langle 111 \rangle$  dislocation glide-controlled plasticity

mechanism [17,18]. These results raise new questions, especially regarding the absence of strain hardening in the tensile stress–strain curves. Customary heavy cold-working processing steps further complicate the matter: giant faults are mainly reported in as-annealed tensile specimens [1–4], whereas studies on dislocation activity were performed on cold-swaged or cold-compressed samples [11–18]. These diverging observations motivated us to conduct a systematic multiscale analysis of deformation mechanisms in gum metal, specifically addressing the contributions of giant faults and lattice dislocations, respectively, to the plastic deformation.

For the experiments, we use a laboratory-cast Ti–22.6Nb–0.47Ta–1.85Zr–1.34O (at.%) alloy. It was produced in an arc-melting furnace under an argon atmosphere and cast into a copper mold. The sample was then annealed for 4 h at 1200 °C and furnace cooled. The chemical composition was controlled by inductively coupled plasma and optical emission spectrometry and infrared absorption measurements. When processing conditions are not properly optimized, Ti–Nb alloys can suffer significantly from segregation and microstructural heterogeneity, which would then play a direct role in deformation characteristics. In this work, to avoid such issues, microstructural and chemical homogeneity were verified by subsequent light microscopy, electron backscatter diffraction (EBSD) and energy dispersive X-ray spectroscopy (EDX) analyses. The alloy was not subjected to any cold-working, to enable unbiased identification of the prevalent deformation mechanisms. EBSD measurements revealed that the microstructure

\* Corresponding author. Tel.: +49 2116792866; e-mail addresses: [c.tasan@mpie.de](mailto:c.tasan@mpie.de); [c.tasan@tue.nl](mailto:c.tasan@tue.nl)

consists of non-textured equiaxed  $\beta$ -phase grains of  $\sim 60 \mu\text{m}$  average size. Small amounts of additional microstructural constituents were also observed by EDX and TEM, i.e. carbide inclusions from casting and  $\omega$  phase from the final cooling. The existence of  $\omega$  phase in gum metal was also reported in recent works (e.g. [4]), although not reported originally (i.e. [1]).

Dog-bone-shaped tensile samples, with gauge dimensions of  $4 \times 2 \times 1 \text{ mm}^3$ , were produced by spark erosion. One surface of the tensile samples was polished prior to the deformation experiment, for postmortem deformation trace analysis. A speckle pattern was applied on the other surface of the specimens for local strain field measurements. Mechanical tests were carried out on a Kammrath and Weiss tensile stage with an initial strain rate of  $5 \times 10^{-4} \text{ s}^{-1}$ , while images were captured with a single camera and correlated afterwards using digital image correlation (DIC) using Aramis software (GOM GmbH, Germany). For some samples, images of the polished surface were captured with a stereomicroscope to correlate the evolution of deformation traces with the global stress–strain curve.

Following the mechanical tests, the deformation-induced microstructure evolution was analyzed at locations of known (i.e. DIC mapped) local strain levels, employing: (i) light microscopy (LIMI) for postmortem analysis of specimen cross-sections; (ii) scanning electron microscopy (SEM) for deformation trace analyses on pre-polished surfaces, as well as EBSD analysis of specimen cross-sections; and (iii) transmission electron microscopy (TEM) for high-resolution morphological and diffraction analysis of deformation structures.

For LIMI and SEM analyses, specimen surfaces were prepared using conventional metallographic grinding, polishing and etching steps. It was observed that finalizing the preparation protocol with  $2 \times 10 \text{ min}$  of colloidal silica polishing (30%  $\text{H}_2\text{O}_2$  solution), followed by 15 s of etching (15%  $\text{NH}_3$ , 15%  $\text{HF}$ , glycerin mixture) provided a deformation-free surface. SEM analyses were carried out using a Zeiss-Crossbeam XB 1540 FIB-SEM instrument (Carl Zeiss SMT AG, Germany) at an accelerating voltage of 15 kV. This instrument is also equipped with an EDAX/TSL system (Draper, UT, USA) used for the EBSD measurements. For TEM analyses, discs with a diameter of 3 mm were cut via wire erosion and mechanically ground to a thickness of 80–90  $\mu\text{m}$ . The discs were then electropolished (Struers Tenupol) at  $-30 \text{ }^\circ\text{C}$  until perforation using an electrolyte of 10% sulfuric acid in methanol. Observations were conducted using a CM20 microscope with a LaB6 cathode at an accelerating voltage of 200 kV.

Finally, small strips ( $4 \times 9 \times 1 \text{ mm}^3$ ) of the gum metal were deformed using an in situ deformation setup that was placed inside the Zeiss microscope. This approach enabled us to conduct electron channeling contrast imaging (ECCI) of the crystallographic defects during deformation [19].

We start our analysis by studying the global mechanical stress–strain response of the tested material. The tensile curve presented in Figure 1 shows that the alloy behaves as a typical non-cold-worked gum metal [3,4,17], with a yield stress close to 650 MPa; hardening-free nominal stress–strain response; and yet an elon-

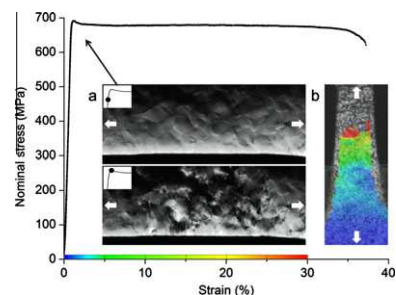


**Figure 1.** Typical stress–strain curve of as-cast and homogenized Ti–22.6Nb–0.47Ta–1.85Zr–1.34O (at.%) gum metal samples (2 mm wide). Inset (a) presents two stereomicroscopy images of a pre-polished surface during deformation. Inset (b) shows the surface strain field calculated by digital image correlation at the point of failure.

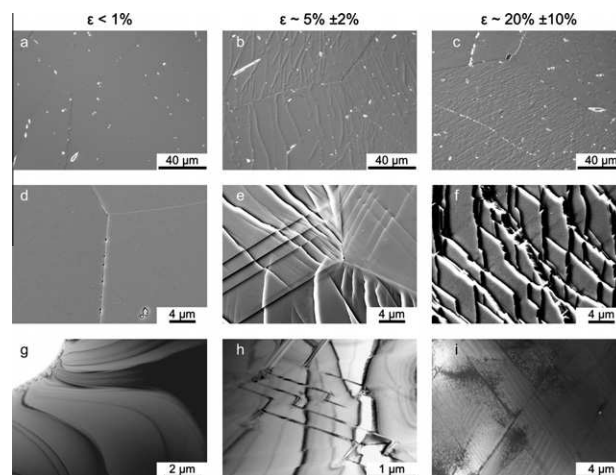


**Figure 2.** Overview of the deformation-induced microstructure evolution in gum metal: light-microscopy images of etched cross-sections (first row), secondary electron images of pre-polished surfaces (second row) and TEM bright-field observations (third row). The uncertainty in the strain measurement at high deformation levels is due to grain roughening, see Figure 1a.

gation to failure above 35%. The small stress peak at the beginning of the plastic regime is a feature also observed by Saito et al. in their pioneering paper [1].

At the onset of plasticity, a significant density of local deformation zones appears on the pre-polished surface. Figure 1a presents two stereomicroscopy images taken during an in situ straining experiment, where the surface roughening becomes clearly visible.<sup>1</sup> To obtain more insights into the nature and evolution of the surface steps created, the microstructure was investigated at locations of known deformation. Strain fields calculated by DIC (Fig. 1b) were used to select these specific locations. Figure 2 presents LIMI (first row), SEM (second row) and TEM (third row) observations of the microstructure at three distinct deformation levels.

These observations reveal the unusual nature of the deformation steps observed at the onset of plasticity

<sup>1</sup>Note that the grain-scale relief already present in the upper image arises from elastic distortions only.

(Fig. 1a). The steps (Fig. 2e) are associated with faults in the bulk material (Fig. 2b), which are similar in morphology to the giant faults reported in the literature [1–4]. On the one hand, the size of the surface steps (Fig. 2e) and the sensitivity to chemical etching of the associated faults (Fig. 2b) suggest that the steps are not dislocation slip traces. Furthermore, in contrast to the continuous lattice rotations observed in dislocation plasticity, large-area EBSD measurements carried out before and after deformation (not shown here) reveal only localized misorientations. On the other hand, the wavy morphology of the surface steps (Fig. 2e) and the small misorientations associated (e.g. Fig. 3b) further indicate that these faults are not mechanical twins typically observed in Ti–Nb–Ta–Zr alloys [17,20], or localized shear bands.

The number of faults increases with deformation, accentuating their role as the governing plasticity mechanism (see Fig. 2c and f). To perceive the physical nature of these features and to assess if any dislocations are present and active, TEM analyses are carried out.

Detailed TEM investigations show no significant dislocation density in the underformed state (Fig. 2g) and at low deformation levels (Fig. 2h). Note that the absence of dislocations is further verified by ECCI analyses showing no dislocation network on etched surfaces (not shown). TEM observations also reveal that each of the faults (such as those in Fig. 2b and e) possesses a lamellar-like structure composed of parallel  $\{112\}\{111\}$   $\beta$  nanotwins (Fig. 2h). Moreover, selected-area diffraction analyses carried out over a single fault show deformation-induced  $\omega$ -phase formation accompanying the mechanical twinning (see key diagram in Fig. 3a).

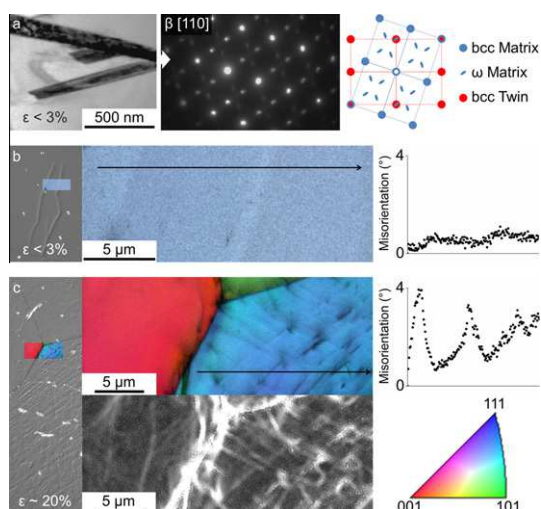


**Figure 3.** (a) TEM bright-field image of a single fault, the diffraction pattern through the width of the fault and its key diagram (adapted from Ref. [4]). (b and c) EBSD observations of (b) two single faults and (c) a highly deformed microstructure. Left parts of (b and c) are composed of light microscopy images of etched cross-sections. Central parts show inverse pole figure maps with a EBSD image-quality map overlay. For (c), a kernel average misorientation map constructed using third neighbor correlations is also displayed with a greyscale span of  $1^\circ$  (bottom row). Right parts show misorientation profiles along the same length (see the black arrows in the inverse pole figure maps).

High-resolution TEM observations of similar twin/ $\omega$ -phase lamellae can be found in the work of Xing and Sun [12].

Altogether, these observations demonstrate that the plasticity is governed by mechanical twinning rather than by “bulk crystal shearing” as suggested by earlier works [1]. Despite this point, we choose to call these defects “giant faults” in this text to maintain a common terminology with the literature.<sup>2</sup>

Dislocations do appear at higher deformation, as shown in Figure 2i, where tilting experiments are performed in the TEM proving a high density of dislocations after 20% plastic deformation. This is somewhat surprising, not only due to the absence of dislocations at lower strains, but also due to the absence of any associated strain hardening in the stress–strain curve in this deformation regime (Fig. 1). Note, however, that “blocks” of giant fault structures are formed at this high deformation level (as shown in the bright-field image of the giant fault arrangement in Fig. 2i). The length scale of these blocks also fits with the cellular structure revealed by the KAM map in Figure 3c. Indeed, the misorientation profile of Figure 3c records amplitudes of a few degrees in a microstructure strained to 20%. This significant difference in orientation between the blocks must be accommodated by the accumulation of geometrically necessary dislocations (GNDs). Therefore, we suggest that the observed dislocations in Figure 2i are generated mainly to accommodate misorientations between giant fault blocks, and that mechanical twinning (assisted by  $\omega$ -phase transformation) is indeed the governing deformation micromechanism.

While this hypothesis would explain the absence of any additional hardening triggered by dislocation–dislocation interactions in the high-deformation regime of gum metal, it does not fully explain why a dislocation–giant fault strain hardening effect is absent. Therefore, to improve our understanding on the interaction between giant fault structures and dislocations, the propagation of a giant fault in an artificially produced dislocation network is monitored using ECCI. Starting from an undeformed etched sample, where no dislocations are present, we noted that a last step of colloidal silica mechanical polishing creates a surface dislocation network.<sup>3</sup> Some giant faults are then introduced in this network using a three-point bending/straining setup, and their propagation was controlled and visualized in situ.

The results obtained from this analysis are summarized in Figure 4. Every dislocation in the upper picture, mapped via ECCI, can be one-to-one tracked in the bottom picture. This enables us to observe that the

<sup>2</sup>A more suitable description of the mechanism would perhaps be “phase-transformation-assisted nanotwinning” (PRANT).

<sup>3</sup>How these dislocations are created by polishing when other observations suggest that plasticity is governed by the giant fault mechanism in tension is an interesting conflict, and an open question. Taking into account earlier reports where dislocation–plasticity was observed in gum metal in compression [15], and our preliminary in situ compression experiments that revealed dislocation activity, the current hypothesis is that the giant fault mechanism is probably impeded under compressive stress states.

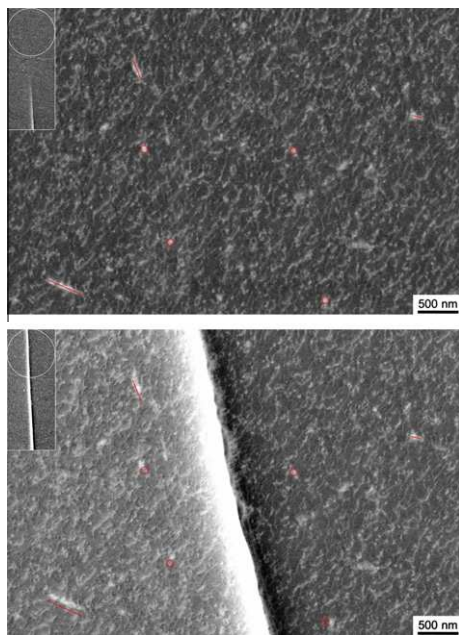


**Figure 4.** Electron channeling contrast imaging of an artificial surface dislocation network before and after the propagation of a giant fault. Insets show lower-magnification pictures of the observed area. Fixed red marks underline the motion associated with the giant fault crossing. (For interpretation of the references to color in this figure legend, the reader is referred to the web version of this article.)

topology of the pre-existing dislocation network is only very weakly affected by the crossing of the giant fault. The change in contrast between the two images is due to the small misorientation associated with the immediate vicinity of the giant fault. The shear caused by the giant fault is documented by the fixed red marks. These results strongly suggest that propagating giant faults, due to their extremely confined character, seem to weakly interact with surrounding dislocation networks.

Based on the multiscale analysis of non-cold-worked gum metal deformed in tension, the following conclusions can be drawn: (i) the giant fault mechanism (which appears to be a phase-transformation-assisted nanotwinning mechanism) governs plasticity of the non-cold-worked gum metal; (ii) dislocations are generated at high plastic strains, apparently to accommodate geometrical misorientations between blocks of giant faults (rather than playing a significant role as carriers of plasticity); and (iii) giant faults are highly localized deformation structures which interact weakly with existing dislocation networks.

While (i) the existence of dislocations after high plastic deformation and (ii) apparent differences in gum metal plasticity in tension vs. compression could explain the conflicting observations in the literature, our ongoing work is on extending the reported analyses to cold-worked Ti–Nb gum metal, in order to obtain a full understanding of gum metal plasticity and giant fault dynamics.

The contributions of M. Adamek in the deformation experiments and postprocessing are acknowledged. E.P. expresses his gratitude to Max-Planck-Institut für Eisenforschung for the scholarship granted to support this work.

- [1] T. Saito et al., *Science* 300 (2003) 464.
- [2] S. Kuramoto, T. Furuta, J.H. Hwang, K. Nishino, T. Saito, *Metall. Mater. Trans. A* 37 (3) (2006) 657.
- [3] T. Furuta, S. Kuramoto, J. Hwang, K. Nishino, T. Saito, *Mater. Trans.* 46 (2005) 3001.
- [4] R.J. Talling, R.J. Dashwood, M. Jackson, D. Dye, *Acta Mater.* 57 (2009) 1188.
- [5] E.A. Withey, A.M. Minor, D.C. Chrzan, J.W. Morris Jr., S. Kuramoto, *Acta Mater.* 58 (2010) 2652.
- [6] R.J. Talling, M. Jackson, R.J. Dashwood, S. Kuramoto, D. Dye, *Scripta Mater.* 59 (2008) 669.
- [7] H. Ikehata, N. Nagasako, T. Furuta, A. Fukumoto, K. Miwa, T. Saito, *Phys. Rev. B* 70 (2004) 174113.
- [8] E.A. Withey, M. Jin, A. Minor, S. Kuramoto, D.C. Chrzan, J.W. Morris Jr, *Acta Mater.* 58 (2010) 2652.
- [9] T. Li, J.W. Morris Jr., N. Nagasako, S. Kuramoto, D.C. Chrzan, *Phys. Rev. Lett.* 98 (2007) 105503.
- [10] M.Yu. Gutkin, T. Ishizaki, S. Kuramoto, I.A. Ovid'ko, N.V. Skiba, *Int. J. Plast.* 24 (2008) 1333.
- [11] W.Y. Guo, H. Xing, J. Sun, X.L. Li, J.S. Wu, R. Chen, *Metall. Mater. Trans. A* 39A (2008) 672.
- [12] H. Xing, J. Sun, *Appl. Phys. Lett.* 93 (2008) 031908.
- [13] H. Xing, J. Sun, Q. Yao, W.Y. Guo, R. Chen, *Appl. Phys. Lett.* 92 (2008) 151905.
- [14] H. Xing, W.Y. Guo, J. Sun, *Trans. Nonferr. Metal. Soc.* 17 (2007) 1456.
- [15] Y. Yang, S.Q. Wu, G.P. Li, Y.L. Li, Y.F. Lu, K. Yang, P. Ge, *Acta Mater.* 58 (2010) 2778.
- [16] Y. Yang, G.P. Li, G.M. Cheng, Y.L. Li, K. Yang, *Appl. Phys. Lett.* 94 (2009) 061901.
- [17] M. Besse, P. Castany, T. Gloriant, *Acta Mater.* 59 (2011) 5982.
- [18] P. Castany, M. Besse, T. Gloriant, *Phys. Rev. B* 84 (2011) 020201.
- [19] I. Gutierrez-Urrutia, S. Zaefferer, D. Raabe, *Scripta Mater.* 61 (2009) 737.
- [20] L. Wang, W. Lu, J. Qin, F. Zhang, D. Zhang, *Mater. Sci. Eng. A* 490 (2008) 421.